



# Statistical properties of a model of a turbulent patch arising from a breaking internal wave

Cite as: Phys. Fluids **33**, 055107 (2021); <https://doi.org/10.1063/5.0046832>

Submitted: 07 February 2021 . Accepted: 09 April 2021 . Published Online: 06 May 2021

T. Katagiri (片桐 崇大),  T. Watanabe (渡邊 智昭), and  K. Nagata (長田 孝二)



View Online



Export Citation



CrossMark

## ARTICLES YOU MAY BE INTERESTED IN

[Impact of numerical hydrodynamics in turbulent mixing transition simulations](#)

Physics of Fluids **33**, 035126 (2021); <https://doi.org/10.1063/5.0034983>

[Qian Jian \(1939–2018\) and his contribution to small-scale turbulence studies](#)

Physics of Fluids **33**, 041301 (2021); <https://doi.org/10.1063/5.0043566>

[Uniform breaking of liquid-jets by modulated laser heating](#)

Physics of Fluids **33**, 044115 (2021); <https://doi.org/10.1063/5.0046915>

**Physics of Fluids**

**SPECIAL TOPIC:** Tribute to  
Frank M. White on his 88th Anniversary

SUBMIT TODAY!

# Statistical properties of a model of a turbulent patch arising from a breaking internal wave

Cite as: Phys. Fluids **33**, 055107 (2021); doi: [10.1063/5.0046832](https://doi.org/10.1063/5.0046832)

Submitted: 7 February 2021 · Accepted: 9 April 2021 ·

Published Online: 6 May 2021





View Online



Export Citation



CrossMark

T. Katagiri (片桐 崇大), T. Watanabe (渡邊 智昭),<sup>a)</sup>  and K. Nagata (長田 孝二) 

## AFFILIATIONS

Department of Aerospace Engineering, Nagoya University, Furo-cho, Chikusa, Nagoya 464-8603, Japan

<sup>a)</sup> Author to whom correspondence should be addressed: [watanabe.tomoaki@c.nagoya-u.jp](mailto:watanabe.tomoaki@c.nagoya-u.jp)

## ABSTRACT

The turbulent patch arising from internal gravity wave breaking is investigated with direct numerical simulation of a stably stratified flow over a two-dimensional hill. The turbulent patch is distinguished from the non-turbulent wave region with potential vorticity. The turbulent patch is highly intermittent, and its location fluctuates with space and time. The buoyancy Reynolds number slowly decays with time in the turbulent patch and the mixing efficiency stays around 0.2. The turbulent patch is separated from the non-turbulent wave region by a turbulent/non-turbulent interfacial (TNTI) layer, whose thickness is about five times the Kolmogorov scale. The kinetic energy dissipation rate also sharply decreases from the turbulent to the wave region while the potential energy dissipation rate has a large peak within the TNTI layer. Both shear and stable stratification are strong in the upper area of the turbulent patch. On the other hand, the lower area has a small mean density gradient, i.e., weak stratification, which is related to the strong intermittency of the turbulent patch in the lower area. Furthermore, weak stratification in the lower area results in a low gradient Richardson number, which is below the critical value for the shear instability, and the roller vortex appears. The outer edge of the turbulent patch aligns with the perimeter of the roller vortex, and the vortex affects the spatial distribution of the turbulent patch.

Published under license by AIP Publishing. <https://doi.org/10.1063/5.0046832>

## I. INTRODUCTION

Turbulent patches are often formed by the breakdown of internal gravity waves in geophysical flows.<sup>1</sup> The turbulent patches are sometimes related to lee waves, which are topographically excited behind an obstacle.<sup>2</sup> Mixing caused by lee waves has a significant influence on the ocean state,<sup>3</sup> where parameters related to the mixing rate, such as turbulent diffusivity and mixing efficiency, are crucial in ocean circulation models.<sup>4</sup> The lee waves excited in the vicinity of mountainous terrain generate flow disturbance, which often creates hazardous flight conditions for aircraft.<sup>5</sup>

The lee waves have been studied with laboratory experiments and numerical simulations, which often consider a simplified and idealized problem of a uniformly stratified fluid. The generation and breaking of lee waves were studied with towing-tank experiments, where an obstacle was towed at a constant speed.<sup>6,7</sup> The wave breaking occurs when the Froude number is sufficiently low although the critical Froude number of the wave breaking depends on the obstacle shape.<sup>6</sup> Numerical simulations were also used to investigate the turbulent patch arising from wave breaking. The towing-tank experiment was compared with direct numerical simulation (DNS) at a low Reynolds number by Gheusi *et al.*,<sup>8</sup> where the wall shear stress was found to have a

significant influence on the formation of the lee wave and its breakdown. DNS of lee waves also revealed that the turbulent patch is sustained by the shear production of turbulent kinetic energy, which approximately balances with dissipation and spatial transport terms.<sup>9</sup>

The turbulent patch arising from the breakdown of internal gravity waves is localized in space, and the location and size of the turbulent patch vary with time. This is the feature of intermittent turbulent flows,<sup>10</sup> where both turbulent and non-turbulent regions are observed. The flow properties are different between the turbulent and non-turbulent regions, which are separated by a thin turbulent/non-turbulent interfacial (TNTI) layer.<sup>10</sup> The intermittent flows are often investigated with an identification scheme of the turbulent region. In non-stratified turbulent flows, the turbulent region is often detected with vorticity.<sup>10</sup> Conditional averages combined with the identification scheme of turbulent regions revealed the turbulent characteristics of intermittent flows. For example, previous studies have used averages taken in the turbulent region<sup>11</sup> and averages taken as a function of the distance from the outer edge of the turbulent region.<sup>10</sup> On the other hand, conventional statistics contain information from both turbulent and non-turbulent regions and do not accurately represent the characteristics of turbulence.

The overall behavior of the turbulent patch is strongly influenced by the intermittency because the turbulent region dominates various flow dynamics. Therefore, the analysis focusing on the intermittent behavior of the turbulent patch helps better understanding the flows associated with the breakdown of internal gravity waves. The turbulent patch is surrounded by internal gravity waves, which are rotational and have non-negligible vorticity. Therefore, the detection of the turbulent patch requires a different method from those used in non-stratified turbulence. The turbulent region of a flow evolving with internal gravity waves is effectively detected with potential vorticity.<sup>12</sup> The method based on the potential vorticity successfully identified the turbulent region of turbulent wakes and turbulent shear layers in a uniformly stratified fluid<sup>12,13</sup> and active turbulent regions of statistically steady, stably stratified homogeneous turbulence.<sup>14</sup> This paper reports a DNS study on the turbulent patch arising from the breakdown of lee waves, where the turbulent patch is identified with the potential vorticity. Statistical properties of turbulence are investigated by taking averages in the detected turbulent region. Furthermore, the flow near the edge of the turbulent patch is studied with the conditional analysis of the TNTI layer.

The paper is organized as follows. The details of DNS are presented in Sec. II. The present DNS is validated by comparisons with other DNS and experiments in Sec. III A. The detection of the turbulent patch is discussed in Sec. III B. Statistical analyses of the turbulent patch are presented in Secs. III C–III F. Finally, the conclusion is presented in Sec. IV.

## II. DNS OF A BREAKING INTERNAL WAVE IN A STRATIFIED FLOW OVER A TWO-DIMENSIONAL HILL

### A. A stratified flow over a two-dimensional hill

DNS is performed for a stably stratified flow over a two-dimensional cosine-shaped hill shown in Fig. 1. Lee waves are generated by the hill, and the Rayleigh–Taylor instability causes wave breaking, which leads to the formation of a turbulent patch.<sup>15</sup> Streamwise, spanwise, and vertical positions in the Cartesian coordinate system are denoted by  $\tilde{x}$ ,  $\tilde{y}$ , and  $\tilde{z}$ , respectively, while the velocity components in these directions are  $\tilde{u}$ ,  $\tilde{v}$ , and  $\tilde{w}$ . Here, the tilde represents a dimensional variable. The origin of the coordinate system is located at the bottom center of the computational domain. We also denote velocity in the  $i$ th direction, pressure, time, and density by  $\tilde{u}_i$ ,  $\tilde{p}$ ,  $\tilde{t}$ , and  $\tilde{\rho}$ , respectively. For simplicity,  $i = 1, 2$ , and 3 represent

the  $x$ ,  $y$ , and  $z$  directions, respectively. The density field  $\tilde{\rho}(\tilde{x}, \tilde{y}, \tilde{z}; \tilde{t})$  is expressed as  $\tilde{\rho}(\tilde{z}) + \tilde{\rho}'(\tilde{x}, \tilde{y}, \tilde{z}; \tilde{t})$ , where  $\tilde{\rho}(\tilde{z})$  is the uniformly stratified background density profile with a constant and negative  $d\tilde{\rho}/d\tilde{z}$  and  $\tilde{\rho}'$  is the perturbation from  $\tilde{\rho}$ .  $d\tilde{\rho}/d\tilde{z}$  is independent of time and treated as a parameter.  $\tilde{\rho}$  can be written as  $\tilde{\rho}_a + (d\tilde{\rho}/d\tilde{z})\tilde{z}$  with a constant  $\tilde{\rho}_a$ . The hill has a two-dimensional geometry, whose local elevation  $\tilde{z}_h$  is given as a function of  $\tilde{x}$

$$\tilde{z}_h(\tilde{x}) = \frac{h_0}{2} \left[ 1 + \cos \left( \pi \frac{\tilde{x}}{a} \right) \right] \quad (|\tilde{x}| \leq a), \quad (1)$$

where  $h_0$  is the height of the hill,  $a = \pi h_0$  is half of the horizontal length of the hill. With Eq. (1), the two-dimensional hill is located at the bottom center of the computational domain. The size of the computational domain is  $(L_x, L_y, L_z) = (100h_0, 10h_0, 10h_0)$  and the domain is defined by  $-L_x/2 \leq \tilde{x} \leq L_x/2$ ,  $-L_y/2 \leq \tilde{y} \leq L_y/2$ , and  $0 \leq \tilde{z} \leq L_z$ . A slip boundary condition is applied to the entire top boundary and the bottom boundary with  $|\tilde{x}| > a$  while a non-slip boundary condition is imposed on the hill ( $|\tilde{x}| \leq a$ ) with an immersed boundary method explained below. An inflow boundary condition with a uniform velocity of  $(\tilde{u}, \tilde{v}, \tilde{w}) = (U_0, 0, 0)$  and zero density perturbations  $\tilde{\rho}' = 0$  is applied at  $\tilde{x} = -L_x/2$  while the convective boundary condition with viscous terms<sup>16</sup> is applied at  $\tilde{x} = L_x/2$ . A periodic boundary condition is used in the spanwise direction. The mixed slip and non-slip boundary conditions on the bottom wall were also used in previous numerical studies.<sup>9,17</sup> It was shown that the lee-wavelength in DNS with the mixed boundary conditions quantitatively agrees with the results of towing-tank experiments.<sup>9</sup> If the entire bottom wall is treated with the non-slip boundary condition, the boundary layer on the wall has to be resolved. Therefore, the computational cost becomes lower when the bottom wall except the hill surface is treated with the slip boundary condition. In towing-tank experiments,<sup>7</sup> the boundary layer develops behind the hill which is towed at a constant speed. In numerical studies, the towing-tank experiments are often approximated by a uniform flow passing the hill fixed on the bottom wall. The slip boundary condition in the upstream region of the hill is reasonable because the boundary layer does not develop in front of the hill in the towing-tank experiments, where the boundary layer develops behind the hill. However, the wave-breaking region is outside the boundary layer. Therefore, even if the non-slip boundary condition is used only on the hill surface, the wave-breaking process

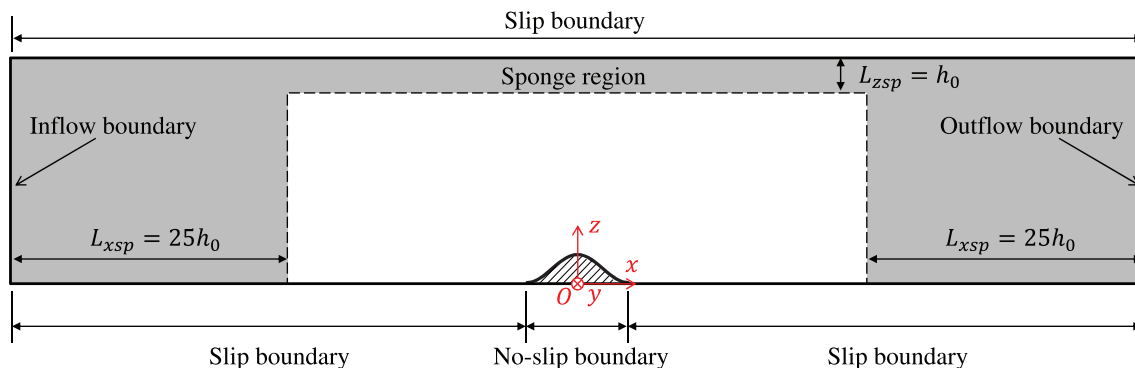


FIG. 1. A schematic of the computational domain of DNS. The gray color represents a sponge zone.

and the size and location of the turbulent patch are consistent between the DNS and experiments.<sup>7,9</sup> If the entire bottom wall including the hill surface is treated with the slip boundary condition, the flow behavior is completely different from realistic lee waves. Laboratory experiments observed the separation bubble (downwind rotor) on the leeward of the hill,<sup>7</sup> and the separation bubble has strong influences on the behavior of the lee wave. When the slip boundary is used for the entire bottom wall, this separation bubble does not appear in numerical simulations.<sup>8</sup> The separation bubble is generated by the friction on the hill surface.<sup>9</sup> Therefore, as long as the non-slip boundary condition is used on the hill, the behavior of the turbulent patch above the hill is qualitatively similar between numerical simulations and laboratory experiments.<sup>7,9</sup> Our DNS results presented in Sec. III A also confirm the formation of the separation bubble, and the visualized turbulent patch is similar to that in the laboratory experiments.<sup>7</sup> The influences of the slip boundary conditions applied away from the hill may affect the flow in the downstream region far away from the hill. However, the present study analyzes the wave-breaking region located above the hill.

The governing equations are Navier–Stokes equations with Boussinesq approximation. The position, time, velocity, density, and pressure are non-dimensionalized as follows:

$$x_i = \frac{\tilde{x}_i}{h_0}, \quad t = \frac{\tilde{t}}{h_0/U_0}, \quad u_i = \frac{\tilde{u}_i}{U_0}, \quad \rho = \frac{\tilde{\rho}}{h_0(-d\tilde{\rho}/d\tilde{z})}, \quad p = \frac{\tilde{p}}{\rho_0 U_0^2}, \quad (2)$$

where  $\rho_0$  is the fluid density that appears as a fluid property in the governing equations. Other variables used in this paper are also normalized with the same reference variables. The governing equations are written with the non-dimensional variables as

$$\frac{\partial u_j}{\partial x_j} = 0, \quad (3)$$

$$\frac{\partial u_i}{\partial t} + \frac{\partial u_i u_j}{\partial x_j} = -\frac{\partial p}{\partial x_i} + \frac{1}{Re} \frac{\partial^2 u_i}{\partial x_j^2} - \frac{1}{Fr^2} \rho' \delta_{i3}, \quad (4)$$

$$\frac{\partial \rho'}{\partial t} + \frac{\partial u_j \rho'}{\partial x_j} = \frac{1}{RePr} \frac{\partial^2 \rho'}{\partial x_j^2} + w, \quad (5)$$

where  $\delta_{ij}$  is the Kronecker's delta. The non-dimensional parameters in the governing equations are the Reynolds number  $Re$ , Prandtl number  $Pr$ , and Froude number  $Fr$

$$Re = \frac{U_0 h_0}{\nu}, \quad Pr = \frac{\nu}{\kappa}, \quad Fr = \frac{U_0}{h_0 N_b}, \quad (6)$$

where  $\nu$  is the kinematic viscosity,  $\kappa$  is the diffusivity coefficient, and  $N_b = \sqrt{(g/\rho_0)(d\tilde{\rho}/d\tilde{z})}$  is the buoyancy frequency of the uniformly stratified fluid with the gravitational acceleration  $g$ . DNS is performed for  $Re = 2000$ ,  $Pr = 1$ , and  $Fr = 0.6$ . The breakdown of lee waves occurs for sufficiently high  $Re$  and low  $Fr$ . The present Reynolds number is higher than the critical Reynolds number for the instability of the lee waves with  $Pr = 1$ , which is in the range of  $100 \lesssim Re \lesssim 500$ . Furthermore, the lee waves with  $Fr = 0.6$  result in the wave breaking regardless the shape of a two-dimensional hill.<sup>6</sup> For this reason,  $Fr = 0.6$  has widely been used in numerical simulations of wave breaking in the existing literature.<sup>7–9</sup>

DNS is initialized with a uniform velocity  $(\tilde{u}, \tilde{v}, \tilde{w}) = (U_0, 0, 0)$  with  $\tilde{\rho}' = 0$ . In numerical simulations of turbulence generated by flow

instabilities, the turbulent transition is usually triggered by adding small perturbations in the flow.<sup>13</sup> We employ the method used in Ref. 9, which superimposes density perturbations on the density field. Time is advanced until  $t = 7.5$ , by which lee waves are formed in the computational domain. At this time instance,  $\rho'$  in the entire computational domain is superimposed by density fluctuations generated by uniform random numbers with a maximum amplitude of 0.02. The density fluctuations result in the wave breaking, and the turbulent patch is generated as discussed in Sec. III.

## B. Numerical methods

The DNS code used in this study is based on finite difference methods. This code was also used in DNS of stably stratified turbulent shear layers<sup>13,18</sup> and turbulent boundary layers and turbulent planar jets without density stratification.<sup>19,20</sup> Spatial discretization is based on a second-order central difference scheme, and time is advanced with a third-order Runge–Kutta method. The Poisson equation for pressure is solved with the Bi-CGStab method.<sup>21</sup>

DNS uses a Cartesian grid with the number of grid points of  $(N_x, N_y, N_z) = (5100, 1150, 1650)$ . The grid points are uniformly spaced in the  $y$  direction. The locations of the grid points in the  $x$  and  $z$  directions are determined by

$$\tilde{x}(i) = -\frac{L_x}{2\alpha_x} \tanh \left[ \tanh(\alpha_x) \left( 1 - 2 \left( \frac{i-1}{N_x-1} \right) \right) \right] \quad \text{with } i = 1, \dots, N_x, \quad (7)$$

$$\tilde{z}(k) = -\frac{L_z}{\tanh(\alpha_z)} \tanh \left[ \alpha_z \left( 1 - \frac{k-1}{N_z-1} \right) \right] + L_z \quad \text{with } k = 1, \dots, N_z, \quad (8)$$

with the grid stretching parameters  $\alpha_x = 4$  and  $\alpha_z = 1$ . These functions provide finer grid spacing near the hill. The smallest length scale of turbulence is evaluated by the Kolmogorov scale. In the fully developed turbulent patch, the Kolmogorov scale normalized by  $h_0$  is about  $7 \times 10^{-3}$ , which hardly varies with time. Section III E also discusses the Kolmogorov scale, which is compared with the Ozmidov scale of the turbulent patch. The grid size in the turbulent patch is about 0.5 times the Kolmogorov scale, which is small enough to resolve small-scale turbulence.

The boundary conditions on the hill surface are imposed with an immersed boundary method. The grid points are classified into fluid points, solid points, and boundary points. The fluid points are located above the hill. The remaining grid points are the boundary points or solid points: the boundary points are the adjacent points of the hill surface while the solid points are the grid points classified as neither fluid nor boundary points. The governing equations are solved for the fluid and boundary points, where additional forcing terms  $f_i$  are added to the momentum equations at the boundary points. The forcing term is expressed as

$$f_i = -(RHS)_i + \frac{u_i^{n+1} - u_i^n}{\Delta t}, \quad (9)$$

$$(RHS)_i = -\frac{\partial u_i u_j}{\partial x_j} - \frac{\partial p}{\partial x_i} + \frac{1}{Re} \frac{\partial^2 u_i}{\partial x_j^2} - \frac{1}{Fr^2} \rho' \delta_{i3}, \quad (10)$$

where  $(RHS)_i$  is the sum of advection, pressure, viscous, and buoyancy terms of the momentum equation in the  $i$ th direction. The superscripts



$n$  and  $n+1$  denote values at  $n$  and  $n+1$  time steps, respectively. After the time integration, the velocity defined at the boundary point becomes  $u_i^{n+1}$ . The value of  $u_i^{n+1}$  is determined with the ghost cell method in Ref. 22, which provides  $u_i^{n+1}$  that satisfies the non-slip boundary condition on the hill surface. It should be noted that the primary interest of this study is the turbulent patch generated above the hill, and the flow attached to the wall is not investigated. The behavior of the turbulent patch above the hill is not sensitive to how the boundary conditions on the hill are imposed. Therefore, the development of the turbulent patch in the present DNS is similar to DNS results obtained with a further simplified immersed boundary method.<sup>9</sup>

Internal gravity waves propagate in the computational domain. Because of the finite domain size, the waves may reflect at the computational boundaries. As suggested in previous studies on a flow with internal gravity waves,<sup>9</sup> the influence of the wave reflection is eliminated with a sponge region shown with gray in Fig. 1, where the streamwise and vertical extents of the sponge region are  $L_{xsp} = 25h_0$  and  $L_{zsp} = h_0$ , respectively. In the sponge region, a second-order low-pass filter is applied to  $u_i$  and  $\rho'$  at the end of every computational time step.

### III. RESULTS AND DISCUSSION

#### A. Temporal evolution of the turbulent patch

Figure 2 visualizes streamwise velocity  $u$  on a  $x$ - $z$  plane between  $t = 15$  and 30. Internal gravity waves are already formed above the hill at  $t = 15$ . At this time, turbulence in the rotor attached to the wall also exists around  $x = 4$ . The wave breaking occurs around  $t = 25$  at  $(x, z) \approx (3, 2)$ , where velocity fluctuations have smaller characteristic length scales than the waves. This turbulent patch arising from the wave breaking is formed in the region of small velocity, and the instantaneous streamwise velocity can be negative in the turbulent patch.

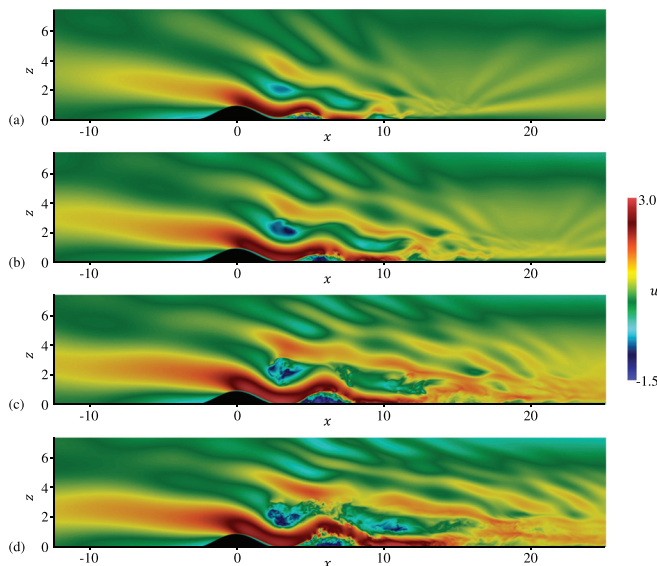


FIG. 2. Wave breaking visualized by streamwise velocity  $u$  on a  $x$ - $z$  plane at (a)  $t = 15$ , (b)  $t = 20$ , (c)  $t = 25$ , and (d)  $t = 30$ .

Figure 3 visualizes streamwise velocity, density perturbations  $\rho'$ , and enstrophy  $\omega^2/2 = (\boldsymbol{\omega} \cdot \boldsymbol{\omega})/2$  at  $t = 70$ , where  $\boldsymbol{\omega}$  is the vorticity vector. At this time, the turbulent patch has fully developed as confirmed from small-scale velocity and density fluctuations in the wave breaking region above the hill. The enstrophy field also exhibits a wave-like pattern especially in the upstream region of the hill because the internal gravity wave induces enstrophy fluctuations by the buoyancy force. The enstrophy profile is very different between the wave region and the turbulent patch. Small-scale patterns in the enstrophy field suggest the existence of small-scale vortices of turbulence.

The present DNS is validated by comparing the temporal evolution of velocity fluctuations with DNS results by Yakovenko *et al.*<sup>9</sup> Following their work, we define velocity variance with a spatial average taken in the rectangular box shown with a white broken line in Fig. 3(c). This box is defined by  $1.25 \leq x \leq 5$  and  $1.25 \leq z \leq 3.75$  and covers the wave-breaking region. The velocity variance is defined as

$$\overline{u_i'^2}(t) = \frac{1}{V} \int_{-5}^5 \int_{1.25}^{3.75} \int_{1.25}^5 \left( u_i(x, y, z, t) - \frac{1}{L_y} \int_{-5}^5 u_i(x, y, z, t) dy \right)^2 dx dz dy, \quad (11)$$

where the integral in the spanwise direction is taken over  $L_y$  and  $V = \int_{-5}^5 \int_{1.25}^{3.75} \int_{1.25}^5 dx dz dy$  is the volume of the box. The temporal evolution of  $\overline{u_i'^2}$  defined by Eq. (11) was presented for wave breaking in a stratified flow over a hill in Ref. 9, where the wave breaking is triggered by imposing white noise to the density field at  $t = 7.5$  as in the present DNS. The Reynolds number in Ref. 9 is  $Re = 4000$ , which is larger than the present DNS ( $Re = 2000$ ), while the Froude number and Prandtl number are the same. Figure 4(a) compares the temporal evolution of the velocity variances of three velocity components between the present DNS and Yakovenko *et al.*<sup>9</sup> The velocity variances rapidly increase from  $t \approx 15$  because of the wave breaking. The growth of the

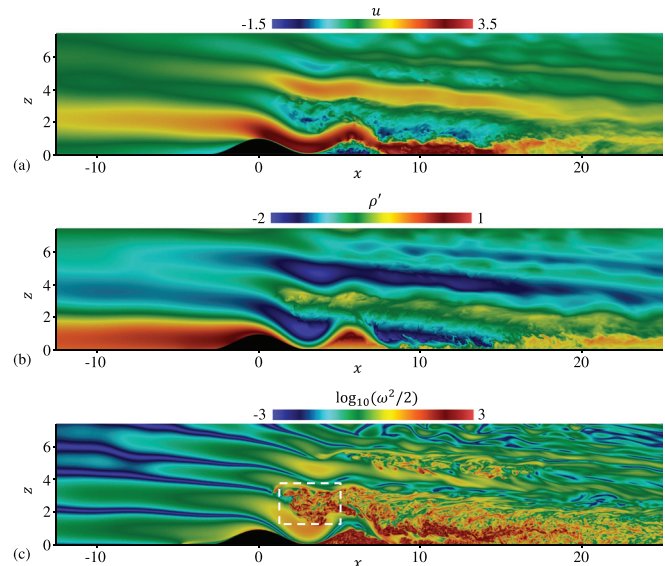
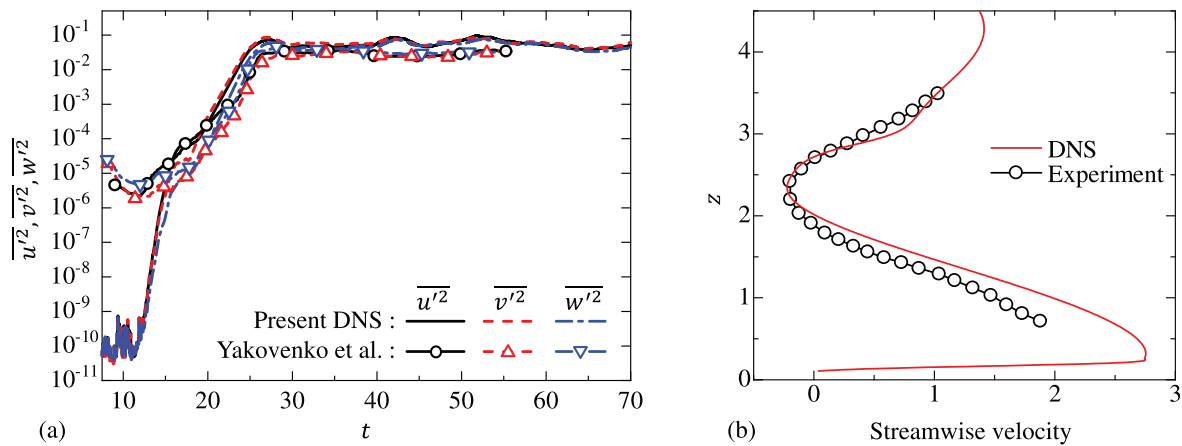


FIG. 3. Flow visualization of a turbulent patch at  $t = 70$ : (a) streamwise velocity  $u$ , (b) density perturbations  $\rho'$ , and (c) enstrophy  $\omega^2/2$ .



**FIG. 4.** (a) Temporal evolution of variances of streamwise velocity  $\overline{u'^2}$ , spanwise velocity  $\overline{v'^2}$ , and vertical velocity  $\overline{w'^2}$  of the wave breaking region calculated with Eq. (11). DNS results by Yakovenko *et al.*<sup>9</sup> ( $Re = 4000$ ) are also plotted for comparison. (b) Vertical profile of streamwise velocity at  $x = 2.7$  in the present DNS and experiment<sup>7</sup> before the turbulent patch fully develops. DNS result shows streamwise velocity averaged in the spanwise direction at  $t = 25$ . The experiment was conducted in a salt-stratified fluid with a towing-tank facility. The Reynolds number in the experiment was  $Re = 580$ .

velocity variances ceases at  $t \approx 27$ , and the turbulent patch is fully developed by this time. A quasi-steady behavior is found for  $t \gtrsim 30$ , and  $\overline{u'^2}$  stays at  $\mathcal{O}(10^{-2})$  until the end of the simulation. The temporal evolution of the velocity variances in the present DNS is consistent with the previous DNS study by Yakovenko *et al.*<sup>9</sup> Qualitative differences between the present DNS and Ref. 9 are possibly caused by different Reynolds numbers. Once the density fluctuations are imposed at  $t = 7.5$ , the fluctuations decay with time before the wave breaking occurs, and this decay is expected to be faster for a lower Reynolds number. Therefore, the velocity variances before the wave breaking in the present DNS are smaller than in Yakovenko *et al.*<sup>9</sup> In the fully developed state ( $t \gtrsim 30$ ), the present DNS yields larger velocity variances. Another DNS study with a small Reynolds number  $Re = \mathcal{O}(10^2)$  reported that velocity variances normalized by  $U_0^2$  are  $\mathcal{O}(10^0)$  in a fully developed turbulent patch.<sup>8</sup> On the other hand, the turbulent patches with  $Re = \mathcal{O}(10^3)$  shown in Fig. 4(a) have  $\overline{u'^2} = \mathcal{O}(10^{-2})$ . Consistently, a comparison between the present DNS ( $Re = 2000$ ) and Yakovenko *et al.* ( $Re = 4000$ )<sup>9</sup> also indicates that the velocity variance becomes larger for lower  $Re$ . Nonetheless, the overall behavior of the wave breaking in the present DNS agrees well with previous DNS studies.<sup>8,9</sup> In this study, the turbulent patch is analyzed for  $t \geq 30$ , for which the velocity variances weakly depend on time.

Figure 4(b) shows the vertical profile of streamwise velocity normalized by  $U_0$  before the turbulent patch fully develops. The present DNS is compared with an experiment conducted in a salt-stratified fluid with a towing-tank facility.<sup>7</sup> Streamwise velocity measured at  $x = 2.7$  with particle image velocimetry is shown in Fig. 4(b), where the streamwise velocity averaged in the spanwise direction in the DNS is also shown. The turbulent patch is formed at a later time between  $1.5 \lesssim z \lesssim 3.5$ . The Schmidt number in the experiment is much larger than 1. The Reynolds number of the experiment was  $Re = 580$ , which is smaller than the present DNS. Nonetheless, the velocity profile agrees well between the DNS and experiment, and the present DNS well reproduces the streamwise velocity profile of the lee wave.

## B. Detection of the turbulent patch

The turbulent patch is detected in the wave-breaking region near the hill, where the turbulence generated by the wave breaking is separated in space from the rotor. Figure 5(a) shows a two-dimensional profile of enstrophy near the hill at  $t = 55$ . The enstrophy distribution has small characteristic length scales in the turbulent patch above the hill and the rotor on the wall, and the difference between the wave region and the turbulent region is noticeable in the enstrophy field. However, the enstrophy level is comparable in the wave and the small enstrophy region in the turbulent patch, and a threshold simply applied to the enstrophy cannot distinguish between the turbulent patch and the internal gravity wave. Following Refs. 12 and 13, we detect the turbulent region with potential vorticity  $\Pi = \omega \cdot \nabla \rho$ . The governing equation of the potential vorticity does not contain terms with the buoyancy force,<sup>12</sup> and the internal gravity wave does not transport the potential vorticity. Therefore, the potential vorticity magnitude  $|\Pi|$  is large in turbulence and small in internal gravity waves outside the turbulence.<sup>12,13</sup> Figure 5(b) visualizes the potential enstrophy  $\Pi^2/2$  in the same area as in Fig. 5(a). The potential enstrophy has large values in the turbulent patch and the rotor while the internal gravity wave outside the turbulence has negligibly small values. Thus, the turbulent patch is well distinguished from the surrounding wave region with the potential vorticity magnitude  $|\Pi|$ .

The turbulent patch is detected with a threshold  $\Pi_{th}$  as the region with  $|\Pi| \geq \Pi_{th}$  while the non-turbulent region with the internal gravity waves is detected as  $|\Pi| < \Pi_{th}$ . An appropriate threshold can be determined by examining the dependence of the turbulent volume on the threshold as suggested in studies on non-stratified turbulence.<sup>23</sup> In this paper, we analyze a rectangular box defined by  $0.3 \leq x \leq 5$ ,  $-5 \leq y \leq 5$ , and  $0.5 \leq z \leq 4$ , where the wave breaking occurs. This box is shown with a white line in Fig. 5(b). The volume of the detected turbulent region,  $V_T$ , is examined in this box for a wide range of  $\Pi_{th}$ . Figure 6 presents  $V_T$  as a function of  $\log_{10} \Pi_{th}$ .  $V_T$  increases from 0 as  $\Pi_{th}$  decreases from  $\log_{10} \Pi_{th} \approx 1$ . This increase in  $V_T$  is due to large

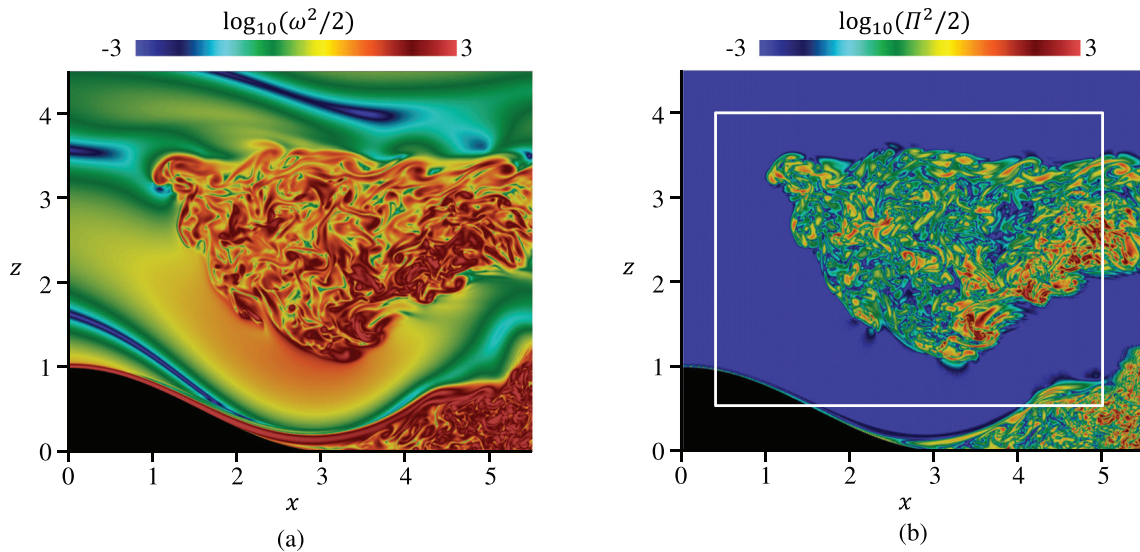


FIG. 5. (a) Enstrophy  $\omega^2/2$  and (b) potential enstrophy  $\Pi^2/2$  in the wave breaking region at  $t = 55$ .

potential vorticity in the turbulent region. Then, there is a small range of  $\log_{10} \Pi_{th}$  where  $V_T$  slowly changes with the threshold for  $\log_{10} \Pi_{th} \approx -1.7$ . The turbulent volume rapidly increases as  $\Pi_{th}$  becomes small for  $\log_{10} \Pi_{th} \lesssim -1.5$ . This is due to the very small  $|\Pi|$  in the wave region outside the turbulent patch. The turbulent and wave regions can be effectively distinguished when the threshold is chosen from a range where  $V_T$  weakly depends on  $\log_{10} \Pi_{th}$ .<sup>23</sup> In practice, we can determine the threshold as  $\Pi_{th}$  that gives the smallest value of  $-dV_T/d\log_{10} \Pi_{th}$ , i.e.,  $d^2V_T/d(\log_{10} \Pi_{th})^2 = 0$ . Figure 6 also marks  $\Pi_{th}$  with the smallest  $-dV_T/d\log_{10} \Pi_{th}$ . This value of  $\Pi_{th}$  is denoted by  $\Pi_{th0}$ , which is used to detect the turbulent patch in this study. It should be noted that the threshold determined based on the turbulent volume has been widely used to detect turbulent regions in various turbulent flows,<sup>13,20,23</sup> and the present DNS further confirms

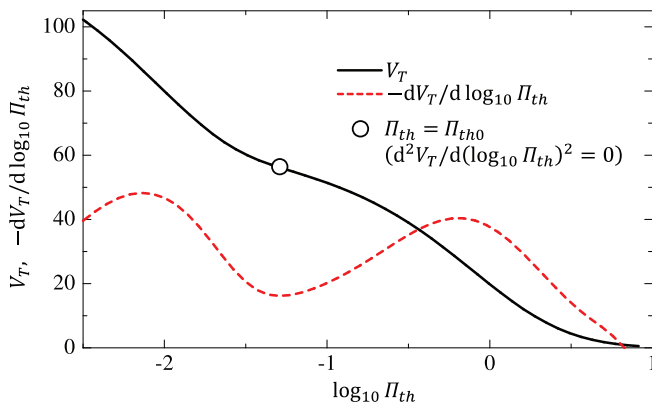


FIG. 6. Dependence of the turbulent volume  $V_T$  on the threshold  $\Pi_{th}$ .  $V_T$  is defined as the volume of the region with  $|\Pi| > \Pi_{th}$  in the rectangular box shown in Fig. 5(b). The circle represents the threshold that satisfies  $d^2V_T/d(\log_{10} \Pi_{th})^2 = 0$ , where  $-dV_T/d\log_{10} \Pi_{th}$  has a local minimum value.

that this method works well for the turbulent patch arising from the wave breaking. The threshold dependence of the turbulent volume is evaluated at each time instance, and the time-dependent threshold is used to detect the turbulent patch.

We introduce an intermittency function  $I(x, y, z, t)$ , which is equal to 1 in the turbulent region and 0 in the non-turbulent region. Figure 7(a) visualizes the detected turbulent region ( $|\Pi| \geq \Pi_{th0}$ ) and the non-turbulent wave region ( $|\Pi| < \Pi_{th0}$ ) with red ( $I = 1$ ) and blue ( $I = 0$ ) colors, respectively. The turbulent patch and rotor are well detected with the present choice of the threshold. There are small noise-like patterns of  $I = 0$  in the turbulent region, whose potential vorticity is smaller than the threshold. These regions are considered as a part of the turbulent patch, and noise-like patterns with  $I = 0$  are removed by the following noise removal procedure. First, a simple moving average of  $I$  is taken with the surrounding 26 grid points. The moving average of  $I$  is denoted as  $I^*$ . Then,  $I$  is calculated again as  $I = 1$  for  $I^* \geq 0.5$  and  $I = 0$  for  $I^* < 0.5$ . The turbulent patch is spatially separated from the rotor turbulence, which appears at the bottom right in Fig. 7(a). Because we intend to detect the turbulent patch arising from the wave breaking,  $I$  is changed to 0 for the turbulent region generated by the rotor on the wall. Figure 7(b) visualizes the turbulent patch detected after this noise removal procedure. Most noise-like patterns are well removed in Fig. 7(b). The turbulent patch arising from the wave breaking has  $I = 1$  and the outside of the patch has  $I = 0$ . The intermittency function  $I$  obtained with these procedures is used to investigate the statistical properties of the turbulent patch in the rest of the paper.

### C. Statistical analysis of the turbulent patch

Two different definitions of averages are used to investigate the turbulent patch. First, we define a volume average in the entire turbulent region as



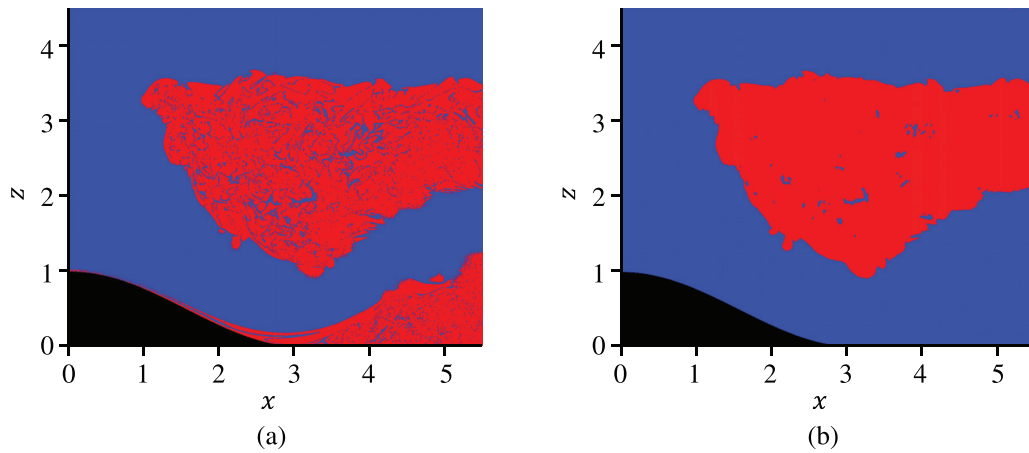


**FIG. 7.** Detection of the turbulent patch: (a) binary image of potential vorticity magnitude  $|\Pi|$  (red:  $|\Pi| > \Pi_{th0}$ ; blue:  $|\Pi| < \Pi_{th0}$ ); (b) detected turbulent patch (red:  $l = 1$ ; blue:  $l = 0$ ).

$$\langle f \rangle_V(t) = \frac{\int_{0.5}^4 \int_{-5}^5 \int_{0.3}^5 I(x, y, z, t) f(x, y, z, t) dx dy dz}{\int_{0.5}^4 \int_{-5}^5 \int_{0.3}^5 I(x, y, z, t) dx dy dz}. \quad (12)$$

The denominator represents the volume of the turbulent region while the numerator is the volume integral of  $f$  in the turbulent region. This average is obtained as a function of time and used to examine the temporal development of the turbulent patch.

Statistical properties near the interface between the turbulent patch and the wave region are also investigated by calculating statistics as functions of a distance from the outer edge of the turbulent patch. The algorithm to calculate the statistics near the interface is the same

as in our previous studies.<sup>20</sup> The outer edge of the turbulent patch is defined as the isosurface of  $|\Pi| = \Pi_{th0}$ . Here, we do not use the isosurface related to the rotor on the wall and the small bubbles of non-turbulent fluid (blue spots surrounded by red in Fig. 7), and the outer boundary of the turbulent patch is used in the analysis of the interface. For a given point on the isosurface of  $|\Pi| = \Pi_{th0}$ , we define a local coordinate  $\zeta_I$ , whose direction is taken in the potential vorticity gradient  $\mathbf{n} = -\nabla|\Pi|/|\nabla|\Pi||$  as shown in Fig. 8(a). The isosurface is located at  $\zeta_I = 0$  and the turbulent and non-turbulent regions appear for  $\zeta_I < 0$  and  $\zeta_I > 0$ , respectively. The local coordinate is uniformly discretized with a spacing smaller than the grid size of DNS. Flow variables defined on the DNS grid are interpolated on the local coordinate with the trilinear interpolation. The interpolation of the variables is

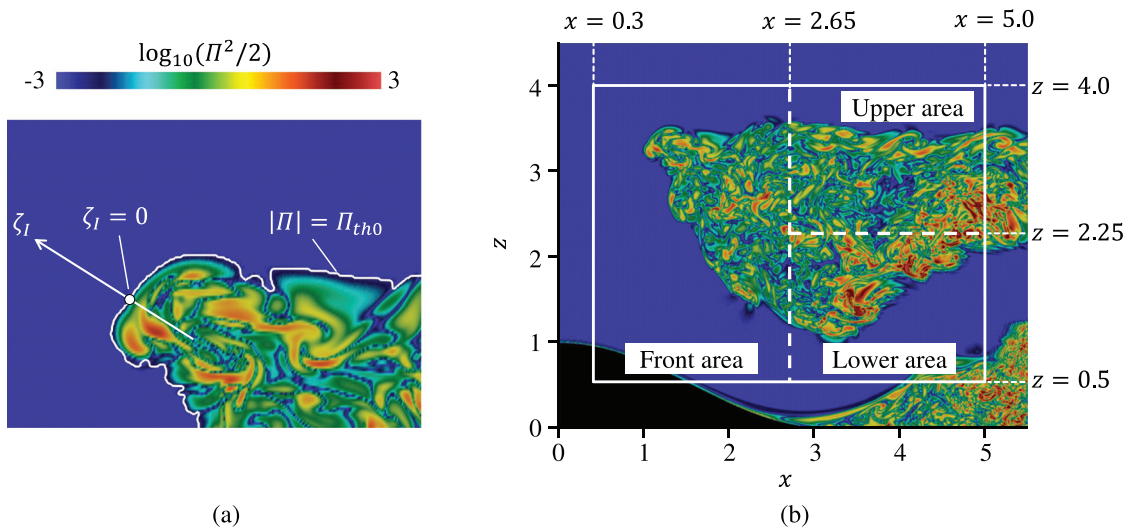


**FIG. 8.** (a) Definition of the local coordinate  $\zeta_I$ . The direction of  $\zeta_I$  is defined with a three-dimensional vector defined with the potential vorticity gradient although  $\zeta_I$  is shown on a two-dimensional plane for the explanation. A white line in (a) represents the isosurface of  $|\Pi| = \Pi_{th0}$ . (b) Three areas for which the statistics near the TNTI layer are separately calculated. A color contour of potential enstrophy is shown in the figures.



repeatedly performed for the local coordinate defined for different locations on the potential vorticity isosurface. Then, one-dimensional profiles of the variables on  $\zeta_I$  are obtained for a large number of the local coordinates, and their ensemble averages are taken as functions of  $\zeta_I$ . This average is denoted by  $\langle \cdot \rangle_I$ . Samples used for this average are obtained between  $t = 45$  and  $65$ . The average concerning the interface is taken to investigate the turbulent patch separately from the non-turbulent region. Therefore, the average for  $\zeta_I < 0$  and  $\zeta_I > 0$  should be calculated solely from the turbulent and non-turbulent regions, respectively. The turbulent region that appears for  $\zeta_I > 0$  is eliminated from statistical samples. Similarly, the non-turbulent region in  $\zeta_I < 0$  is not used to calculate the statistics near the interface. The statistics near the interface are calculated for the entire isosurface of  $|\Pi| = \Pi_{th0}$ . Furthermore, the statistics are calculated for three areas described in Fig. 8(b). The front area is defined by  $0.3 \leq x \leq 2.65$ , while the region of  $x > 2.65$  is divided into two regions: the upper area of  $2.25 \leq y \leq 4.0$  and the lower area of  $0.5 \leq y < 2.25$ .

#### D. Intermittency of the turbulent patch

An average of  $I$  yields an intermittency factor as  $\gamma(x, z) = [(T_2 - T_1)L_y]^{-1} \int_{T_1}^{T_2} \int_{-5}^5 I(x, y, z, t) dy dt$ , which is a probability that the turbulent fluid appears at  $(x, z)$ . Here, time and spanwise averages are taken for  $I$ , where  $T_1 = 45$  and  $T_2 = 65$ . Figure 9(a) shows a color contour of  $\gamma$  while Fig. 9(b) shows vertical profiles of  $\gamma$  at  $x = 2.0, 3.0$ , and  $4.5$ . Large values of  $\gamma$  appear for  $z \approx 3$  and  $x \gtrsim 2$ , where the turbulent fluid frequently appears. However,  $\gamma$  is smaller than 1 in most of the flow, and the turbulent patch is highly intermittent in space and time. In Fig. 9(b),  $\gamma$  rapidly decreases with  $z$  at the top of the turbulent patch compared with the lower side. Therefore, the intermittency is strong in the lower region of the turbulent patch. This difference between the upper and lower regions of the turbulent patch is related to different strengths of stratification in these regions as explained below.

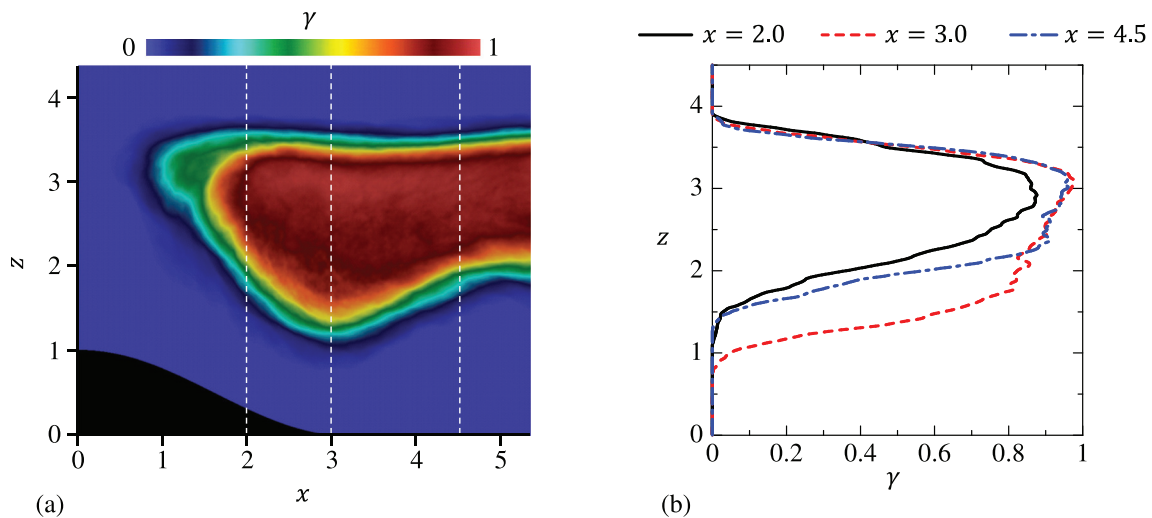


**FIG. 9.** (a) A color contour of intermittency factor  $\gamma$  in the wave breaking region near the hill. (b) Vertical profiles of  $\gamma$  at  $x = 2.0, 3.0$ , and  $4.5$ . These locations are shown with vertical broken lines in panel (a).

#### E. Temporal evolution of statistics in the turbulent patch

Figure 10(a) shows the temporal evolution of the turbulent volume  $\bar{V}_T = \int_{0.5h_0}^{4h_0} \int_{-5h_0}^{5h_0} \int_{0.3h_0}^{5h_0} I(x, y, z, t) d\tilde{x} d\tilde{y} d\tilde{z}$  normalized by  $h_0^2 L_y$ . The turbulent volume fluctuates with time, and it increases until  $t = 55$  and slightly decreases in the late time. This behavior is consistent with the quasi-steady state of the turbulent patch found for velocity variances because the turbulent patch cannot be statistically steady if the turbulent volume monotonically increases. The fluctuations of the turbulent volume indicate strong intermittency of the turbulent patch, and the flow region near the hill becomes turbulent or non-turbulent depending on time.

Root-mean-squared (rms) fluctuations of  $f$  in the turbulent patch are defined as  $f_{rmsV}(t) = \sqrt{\langle f^2 \rangle_V - \langle f \rangle_V^2}$ . Figure 10(b) shows rms fluctuations of velocity components,  $u$ ,  $v$ , and  $w$  and density  $\rho'$ . It was shown that the mean velocity gradient above the hill contributes to the shear production of the turbulent kinetic energy.<sup>9</sup> Therefore, rms velocity fluctuations in the turbulent patch weakly depend on time, and the present DNS yields  $u_{rmsV} \approx 0.45$ ,  $v_{rmsV} \approx 0.32$ , and  $w_{rmsV} \approx 0.29$ . Rms density fluctuations gradually increase with time from  $t = 30$  and slightly decrease after  $t = 60$ . The buoyancy effects of a stably stratified fluid generally damps vertical turbulent motions. However, rms velocity fluctuations in the turbulent patch are comparable for spanwise ( $v$ ) and vertical ( $w$ ) components, and the turbulent motions in the vertical direction are still active in the turbulent patch. The production of density fluctuations is related to the vertical velocity of the last term on the right-hand side of Eq. (5). Therefore, rms density fluctuations in Fig. 10(b) also hardly decay with time because fluctuations in the vertical velocity contribute to the production of density fluctuations.

The smallest scale of turbulent motions is characterized by the Kolmogorov scale, which is defined with the volume average in the turbulent patch as  $\tilde{\eta}_V = (\nu^3 / \langle \tilde{\epsilon} \rangle_V)^{1/4}$ , where  $\tilde{\epsilon} = 2\nu \tilde{S}_{ij} \tilde{S}_{ij}$  is the kinetic energy dissipation rate and  $S_{ij}$  is the rate-of-strain tensor. One of the most important length scales in stably stratified turbulence is

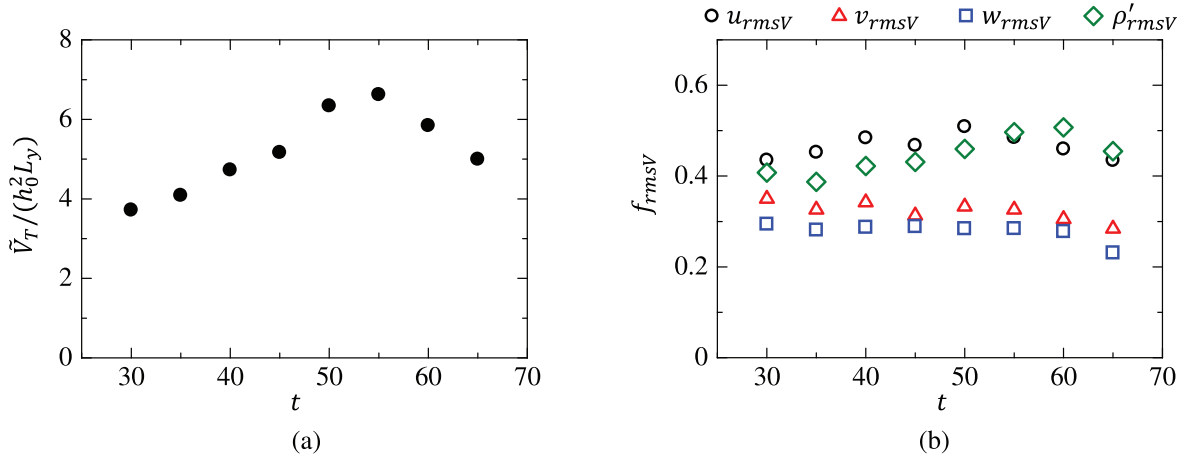


FIG. 10. Temporal evolution of (a) the volume of the turbulent patch normalized by  $h_0^2 L_V$  and (b) rms velocity and density fluctuations in the turbulent patch.

the Ozmidov scale. The turbulent motion at scales greater than the Ozmidov scale is significantly damped in stratified turbulence. The Ozmidov scale  $L_{OV}$  can be defined with the buoyancy frequency  $\tilde{N}_V = \sqrt{-(g/\rho_0)\langle\partial\tilde{\rho}/\partial\tilde{z}\rangle_V}$  as  $\tilde{L}_{OV} = \sqrt{\langle\tilde{\epsilon}\rangle_V/\tilde{N}_V^3}$ . Figure 11(a) shows temporal variations of  $\eta_V$  and  $L_{OV}$ . Both Kolmogorov scale and Ozmidov scale normalized by  $h_0$  weakly depend on time, and the turbulent patch has  $\eta_V \approx 7 \times 10^{-3}$  and  $L_{OV} \approx 2 \times 10^{-1}$ . The relation between the Kolmogorov scale and Ozmidov scale is related to the buoyancy Reynolds number defined as  $Re_{bV} = \langle\tilde{\epsilon}\rangle_V/\nu\tilde{N}_V^2$ , which can also be written as  $Re_{bV} = (L_{OV}/\eta_V)^{4/3}$ . From the definition,  $Re_{bV} \gg 1$  is equivalent to  $L_{OV} \gg \eta_V$ . In this case, active small-scale turbulent motions exist at scales between  $L_{OV}$  and  $\eta_V$ . Figure 11(b) plots the buoyancy Reynolds number against time.  $Re_{bV}$  slowly decays with time. It should be noted that the buoyancy Reynolds number exponentially decays with time in a decaying turbulent shear layer under stable stratification.<sup>13</sup> However,  $Re_{bV}$  in the turbulent patch stays around 60 even at  $t = 65$ , and the decay of  $Re_{bV}$  is very slow compared with other

decaying stably stratified turbulence, e.g., a turbulent wake of a sphere and a turbulent shear layer in a stably stratified fluid.<sup>24,25</sup> The turbulent patch has  $L_{OV} \gg \eta_V$  and  $Re_{bV}$  is large even in the quasi-steady state. Thus, active small-scale turbulence is sustained for a long time period in the turbulent patch.

The mixing efficiency is examined in the detected turbulent patch. The mixing efficiency is the ratio of the net change in the background potential energy to the energy expended in the mixing,<sup>26</sup> and it is often assumed to be 0.2, which is the upper bound considered by Osborn.<sup>27</sup> Various expressions have been used to estimate the mixing efficiency or relevant parameters. Following Ref. 28, the mixing efficiency  $\mathcal{E}_V$  is evaluated as follows:

$$\mathcal{E}_V(t) = \frac{\langle\epsilon_p\rangle_V}{\langle\epsilon\rangle_V + \langle\epsilon_p\rangle_V}, \quad (13)$$

where  $\epsilon_p$  is the dissipation rate of available potential energy, which is defined by  $\epsilon_p = (1/RePrFr^2)(\nabla\rho' \cdot \nabla\rho')$ . Figure 12 plots  $\mathcal{E}_V$  as a function of time. The turbulent patch has  $\mathcal{E}_V \approx 0.2$  with small scatter,

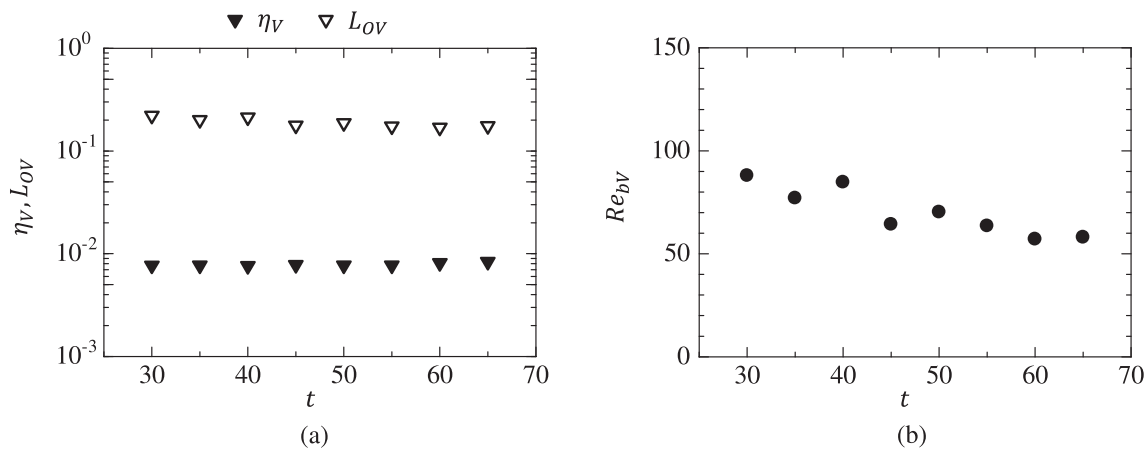


FIG. 11. Temporal variations of (a) Kolmogorov scale  $\eta_V$  and Ozmidov scale  $L_{OV}$  and (b) buoyancy Reynolds number  $Re_{bV}$ .

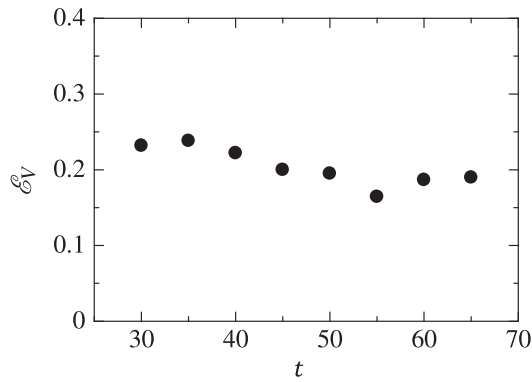


FIG. 12. Temporal variation of mixing efficiency  $\mathcal{E}_V = \langle \varepsilon_p \rangle_V / (\langle \varepsilon \rangle_V + \langle \varepsilon_p \rangle_V)$  in the turbulent patch.

and this value is consistent with the value widely used in oceanography.<sup>26</sup>

### F. Characteristics of the turbulent/non-turbulent interface

Statistics near the TNTI layer are presented as functions of the distance from the outer edge of the turbulent patch. Here, we have calculated the statistics with the entire isosurface of potential vorticity or separately for three areas defined in Fig. 8(b). The present DNS results are compared with DNS of a stably stratified shear layer in a uniformly stratified fluid.<sup>13</sup> Here, the results are taken at nondimensional time of 120 from the DNS with  $Re = 6000$  and  $Fr = 0.6$ , where  $Re = h_S U_S / \nu$  and  $Fr = 2U_S / h_S N_b$  are defined with the initial shear layer thickness  $h_S$  and the velocity jump  $U_S$ . Variables in the stably stratified shear layer are also normalized as Eq. (2), where the length and velocity scales are replaced by  $h_S$  and  $U_S$ , respectively. This DNS data were chosen because the buoyancy Reynolds number is close to the present

DNS. For the present DNS, the local coordinate  $\zeta_I$  is normalized by the Kolmogorov scale  $\eta_V$  in the turbulent patch. For the stably stratified shear layer, the Kolmogorov scale at the center of the shear layer is used for normalization. Because the Kolmogorov scale near the TNTI layer is slightly different from these Kolmogorov scales, the differences in the statistics between these flows can also be attributed to the normalization of  $\zeta_I$ . Furthermore, most results except for non-dimensional parameters are compared qualitatively below because these flows have different characteristic length and velocity scales.

Figure 13 shows the mean profiles of enstrophy  $\langle \omega^2/2 \rangle_I$  and potential enstrophy  $\langle \Pi^2/2 \rangle_I$  near the TNTI layer. Both enstrophy and potential enstrophy decrease across the TNTI layer from the turbulent to non-turbulent region. However, the mean enstrophy is different between these two regions only by a factor of  $\mathcal{O}(10^1)$ . This is because the internal gravity wave around the turbulent patch has enstrophy comparable to weak enstrophy regions in the turbulent patch. The mean potential enstrophy decreases from  $\mathcal{O}(10^0)$  to  $\mathcal{O}(10^{-4})$  across the TNTI layer, and the potential enstrophy effectively distinguishes the turbulent patch from the non-turbulent wave region. The rapid decrease in  $\langle \Pi^2/2 \rangle_I$  occurs for  $-10 \lesssim \zeta_I/\eta_V \lesssim 0$ . The vertical width of the turbulent patch is  $\mathcal{O}(h_0)$  while the Kolmogorov scale is smaller than  $0.01h_0$ . Thus, the turbulent patch has a very thin interfacial layer whose thickness is much smaller than the size of the turbulent patch. These profiles of  $\langle \omega^2/2 \rangle_I$  and  $\langle \Pi^2/2 \rangle_I$  are qualitatively similar in the stably stratified shear layer.<sup>13</sup> Thus, the intermittent turbulent flows in a stably stratified fluid can be divided into three regions: the turbulent region, where both  $\Pi^2/2$  and  $\omega^2/2$  are large, the non-turbulent wave region with moderately large  $\omega^2/2$  and small  $\Pi^2/2$ , and the interfacial layer, where  $\omega^2/2$  and  $\Pi^2/2$  are adjusted between these two regions.

The TNTI layer can be identified on the  $\zeta_I$  axis as the region with a large potential vorticity gradient. The mean thickness of the TNTI layer is estimated with the mean potential vorticity gradient  $\Pi'_I = \partial \langle |\Pi| \rangle_I / \partial \zeta_I$ . Figure 14 presents the mean potential vorticity profile  $\langle |\Pi| \rangle_I$  and its gradient  $\Pi'_I = \partial \langle |\Pi| \rangle_I / \partial \zeta_I$  obtained with the average taken for the entire potential vorticity isosurface. Within the

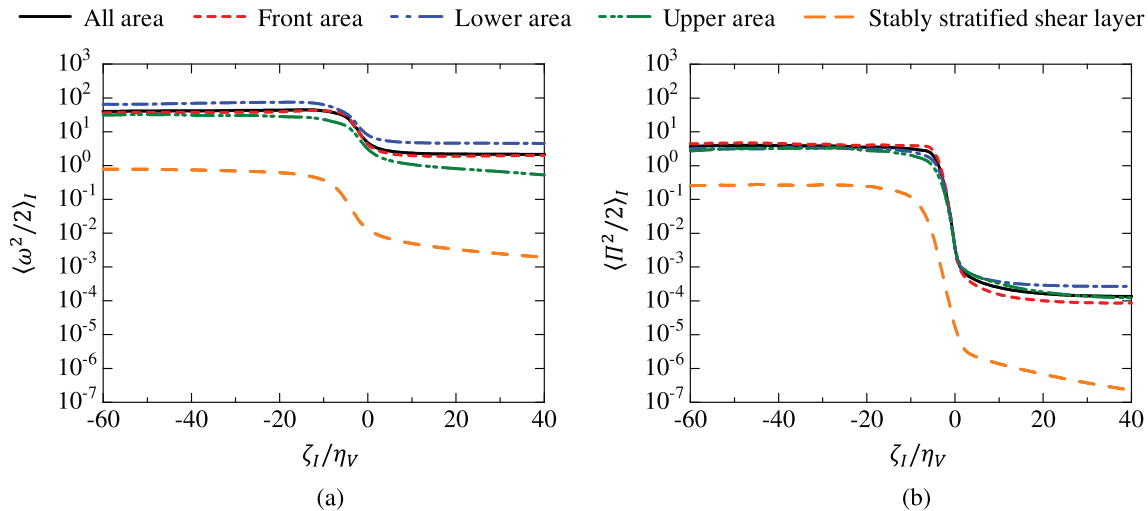


FIG. 13. Averages of (a) enstrophy  $\langle \omega^2/2 \rangle_I$  and (b) potential enstrophy  $\langle \Pi^2/2 \rangle_I$  near the TNTI layer.  $\langle \omega^2/2 \rangle_I$  and  $\langle \Pi^2/2 \rangle_I$  in the stably stratified shear layer<sup>13</sup> are also shown with  $\zeta_I$  normalized by the Kolmogorov scale on the shear layer centerline.

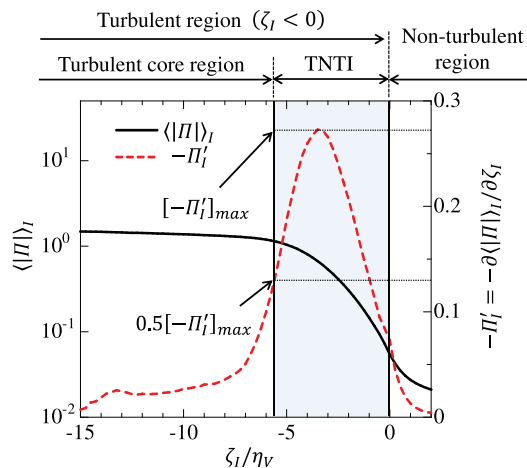


FIG. 14. Estimation of the thickness of the TNTI layer.

TNTI layer,  $-\Pi'_I$  has a peak because the potential vorticity rapidly decreases from the turbulent to non-turbulent region. The thickness  $\delta_I$  is estimated as the distance from  $\zeta_I = 0$  to the location where  $-\Pi'_I$  is equal to half of its maximum value  $[-\Pi'_I]_{max}$  as depicted in Fig. 14. The same method to quantify the thickness was used in previous studies on the TNTI layer.<sup>13</sup> The thickness estimated by this method was compared with the estimation based on the fitting of an error function to the mean potential vorticity profile in Ref. 13, and it was shown that these two methods yield similar thickness. Table I summarizes the TNTI layer thickness normalized by the Kolmogorov scale,  $\delta_I/\eta_V$ . The turbulent patch has the TNTI layer with a thickness of about five times the Kolmogorov scale. This thickness is similar for the front, upper, and lower regions of the turbulent patch, and the interfacial layer has the thickness close to the smallest scale of turbulent motions. Furthermore, it was shown that the TNTI layer thickness is about 10 times the Kolmogorov scale  $\eta$  in turbulent wakes and shear layers in a stably stratified fluid.<sup>12,13</sup> The normalized values of  $\delta_I/\eta$  in these studies slightly vary depending on the location where  $\eta$  is evaluated. The turbulent patch arising from the wave breaking and other turbulent free shear flows in a stably stratified fluid have a thin interfacial layer at the edge of the turbulent region.

The mean vertical shear and buoyancy frequency near the TNTI layer are evaluated as  $S_I = \langle \partial u / \partial z \rangle_I$  and  $N_I = \sqrt{-(g/\rho_0) \langle \partial \tilde{\rho} / \partial z \rangle_I}$ . Figure 15 shows  $S_I$  and  $N_I$  calculated for the TNTI layer in the front, upper, and lower areas. The mean shear exists even in the non-turbulent region ( $\zeta_I > 0$ ), where the wave motions and the flow accelerated over the hill can contribute to the mean velocity gradient. In the turbulent patch ( $\zeta_I < 0$ ), the magnitude of  $S_I$  has a peak at  $\zeta_I \approx -5\eta_V$ , and the shear is stronger near the TNTI layer than in the

turbulent core region. The magnitude of  $S_I$  is larger near the TNTI layer in the lower area than the front and upper areas. In Fig. 15(b), the buoyancy frequency tends to decrease from the non-turbulent toward the turbulent region because the mean density gradient becomes small owing to the mixing of density in the turbulent patch. In the upper region,  $N_I$  has a large peak at  $\zeta_I \approx -5\eta_V$ , and the TNTI layer is strongly stratified. Figure 15 also shows  $S_I$  and  $N_I$  in the stably stratified shear layer. The TNTI layer thickness in the stably stratified shear layer was about 10 times the Kolmogorov scale.<sup>13</sup> Both mean shear and buoyancy frequency are larger in the vicinity of the TNTI layer than in the turbulent core region. The peaks of  $S_I$  and  $N_I$  exist near the boundary between the turbulent core region and the TNTI layer in the stably stratified shear layer. Similarly, the upper area of the turbulent patch exhibits peaks of  $S_I$  and  $N_I$  at  $\zeta_I \approx -5\eta_V$  while the thickness of the TNTI layer is about  $5\eta_V$ . These results imply that the upper area of the turbulent patch is well approximated by a stably stratified turbulent shear layer.  $\tilde{N}_I$  obtained in the front and lower areas does not have a large peak within the TNTI layer, and the stratification is not strengthened near the edge of the turbulent patch. Previous studies on the TNTI layer in a stably stratified fluid found that the intermittency of turbulence is weakened by buoyancy. Stronger stratification results in a narrower intermittent region with  $0 < \gamma < 1$ , where both turbulent and non-turbulent fluids are observed.<sup>29,30</sup> Similarly, the strongly stable stratification with large  $\tilde{N}_I$  in the upper area results in a narrow intermittent region, where  $\gamma$  rapidly decreases with  $z$  in Fig. 9. The lower area with small  $\tilde{N}_I$  has a wider intermittent region of  $0 < \gamma < 1$  than the upper area.

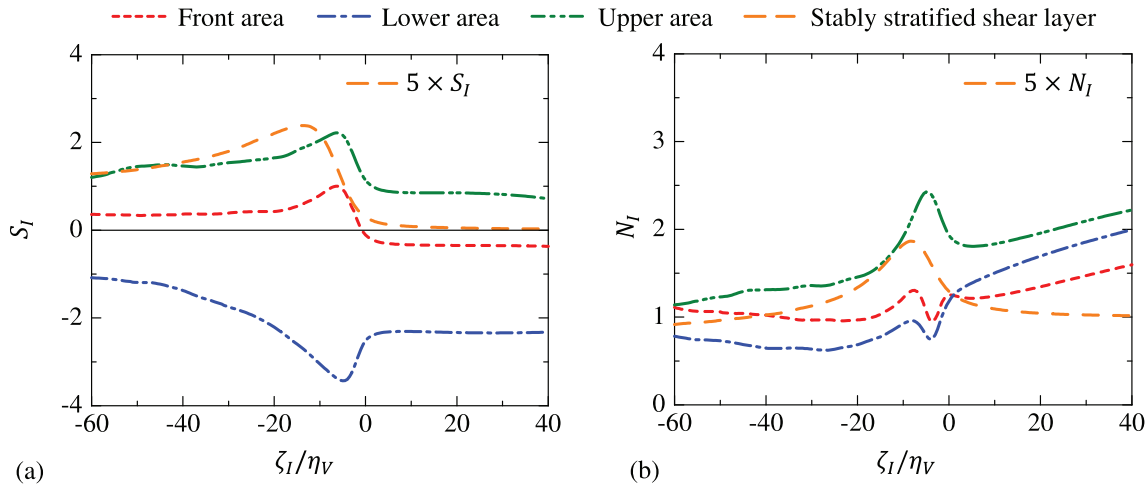
Figure 16 shows the averages of kinetic energy and potential energy dissipation rates, which are calculated as  $\langle \varepsilon \rangle_I$  and  $\langle \varepsilon_p \rangle_I$ , respectively. The dissipation rates rapidly change within the TNTI layer. Although the dissipation rates are small in the non-turbulent region ( $\zeta_I > 0$ ),  $\langle \varepsilon \rangle_I$  and  $\langle \varepsilon_p \rangle_I$  have non-zero values because of the dissipation related to the wave motion and fluid motion induced by turbulence.  $\langle \varepsilon_p \rangle_I$  has a peak within the TNTI layer while a large peak in the kinetic energy dissipation rate does not appear. Figure 16 also shows  $\langle \varepsilon \rangle_I$  and  $\langle \varepsilon_p \rangle_I$  in the stably stratified shear layer.<sup>13</sup> Here, these quantities are multiplied by 100 for comparison with the present DNS because the magnitude of  $\langle \varepsilon \rangle_I$  and  $\langle \varepsilon_p \rangle_I$  is different between the turbulent patch and the stably stratified shear layer. The changes of  $\langle \varepsilon \rangle_I$  and  $\langle \varepsilon_p \rangle_I$  across the TNTI layer are similar in the stably stratified shear layer and the upper and lower areas of the turbulent patch.  $\langle \varepsilon \rangle_I$  and  $\langle \varepsilon_p \rangle_I$  begin to decrease already at  $\zeta_I/\eta_V = -10$  in the stably stratified shear layer because the TNTI layer thickness is about 10 times the Kolmogorov scale. The definition of  $\varepsilon_p$  has the same form as passive scalar dissipation rate, whose profiles near the TNTI layer have been studied in turbulent free shear flows. A large peak of mean passive scalar dissipation rate was also found within the TNTI layer.<sup>31,32</sup> Therefore, the peak found for  $\langle \varepsilon_p \rangle_I$  is attributed to the nature of the scalar dissipation rate. The peak of the potential energy dissipation is the largest in the front area in Fig. 16 although  $\langle \varepsilon_p \rangle_I$  in the turbulent core region is comparable in the front and upper area.

Figure 17(a) shows the buoyancy Reynolds number near the TNTI layer  $Re_{bl} = \langle \tilde{\varepsilon} \rangle_I / \nu \tilde{N}_I^2$ , which rapidly decreases across the TNTI layer toward the non-turbulent region. This behavior of  $Re_{bl}$  is consistent with the absence of small-scale turbulent motions outside the turbulent patch. The profiles of  $S_I$  and  $N_I$  have confirmed that the stably stratified shear layer is formed in the upper area. The profile of

TABLE I. The thickness of the TNTI layer  $\delta_I$  normalized by the Kolmogorov scale of the turbulent patch  $\eta_V$ .

|                   | All area | Front area | Upper area | Lower area |
|-------------------|----------|------------|------------|------------|
| $\delta_I/\eta_V$ | 5.2      | 5.0        | 5.1        | 6.6        |





**FIG. 15.** (a) Mean shear  $S_I$  and (b) buoyancy frequency  $N_I$  near the TNTI layer. Figures also show  $S_I$  and  $N_I$  in the stably stratified shear layer<sup>13</sup> for comparison.  $S_I$  and  $N_I$  in the stably stratified shear layer are multiplied by five to compare their distribution with the turbulent patch.

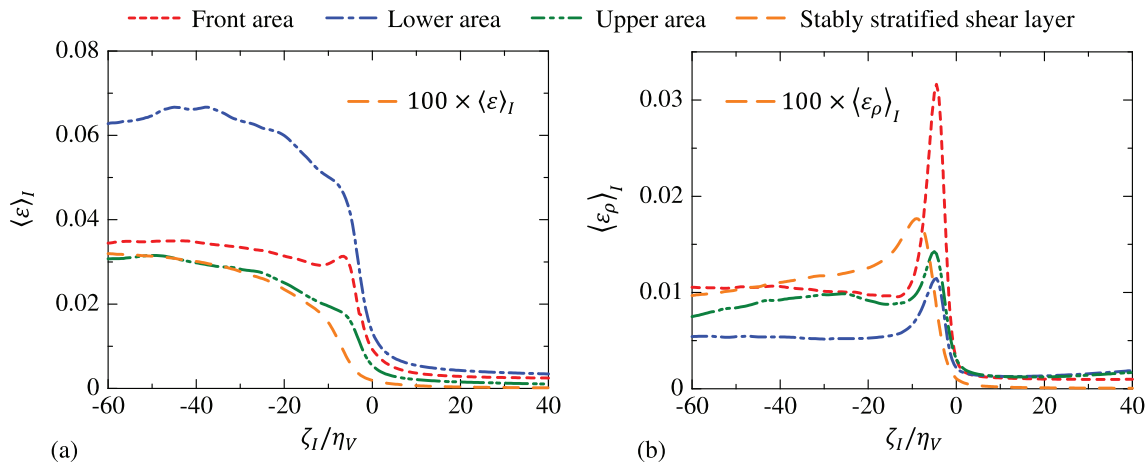


**FIG. 16.** Mean profiles of (a) kinetic energy dissipation rate  $\langle \epsilon \rangle_I$  and (b) potential energy dissipation rate  $\langle \epsilon_\rho \rangle_I$  near the TNTI layer. Figures also show  $\langle \epsilon \rangle_I$  and  $\langle \epsilon_\rho \rangle_I$  in the stably stratified shear layer.<sup>13</sup>

$Re_{bl}$  is also similar between the upper area and the stably stratified shear layer.  $Re_{bl}$  weakly depends on  $\zeta_I$  for  $\zeta_I \lesssim 20$ , where  $Re_{bl} \approx 30$ – $50$ .  $Re_{bl}$  decreases toward the TNTI layer even in the turbulent core region of  $-20 \lesssim \zeta_I/\eta_V \lesssim -5$ . Then,  $Re_{bl}$  further decreases within the TNTI layer. In the lower and front areas,  $Re_{bl}$  in the turbulent region is large even near the TNTI layer, where  $Re_{bl}$  has a peak. Then,  $Re_{bl}$  rapidly decreases within the TNTI layer ( $-5 \lesssim \zeta_I/\eta_V \leq 0$ ). Therefore, the small-scale turbulence is still active even near the TNTI layer in the front and lower areas. This is because the stratification is weak in these areas as confirmed in Fig. 15(b). Thus, the profile of  $Re_{bl}$  near the TNTI layer is not universal and can depend on flows. For example, the flow between the turbulent patch and the hill is accelerated, and the turbulent patch in the lower area is influenced by a large mean velocity gradient. The production of

turbulent kinetic energy by the mean velocity gradient can lead to the large  $Re_{bl}$  in the lower area.

Figure 17(b) presents the gradient Richardson number  $Ri_{gl} = N_I^2/S_I^2$ , which represents the time scale ratio of shear to buoyancy. Larger  $Ri_{gl}$  indicates stronger stratification compared with shear. The figure also shows  $Ri_{gl}$  in the stably stratified shear layer.<sup>13</sup>  $Ri_{gl}$  weakly depends on  $\zeta_I$  in the turbulent core region in the upper area of the turbulent patch and the stably stratified shear layer.  $Ri_{gl}$  sharply increases across the TNTI layer toward the non-turbulent region in both flows.  $Ri_{gl}$  further increases in the non-turbulent region in the stably stratified shear layer because the mean velocity gradient is close to 0 outside the shear layer. However, the mean velocity gradient is caused by the internal gravity wave outside the turbulent patch. Therefore,  $Ri_{gl}$  in the non-turbulent region is smaller in the turbulent

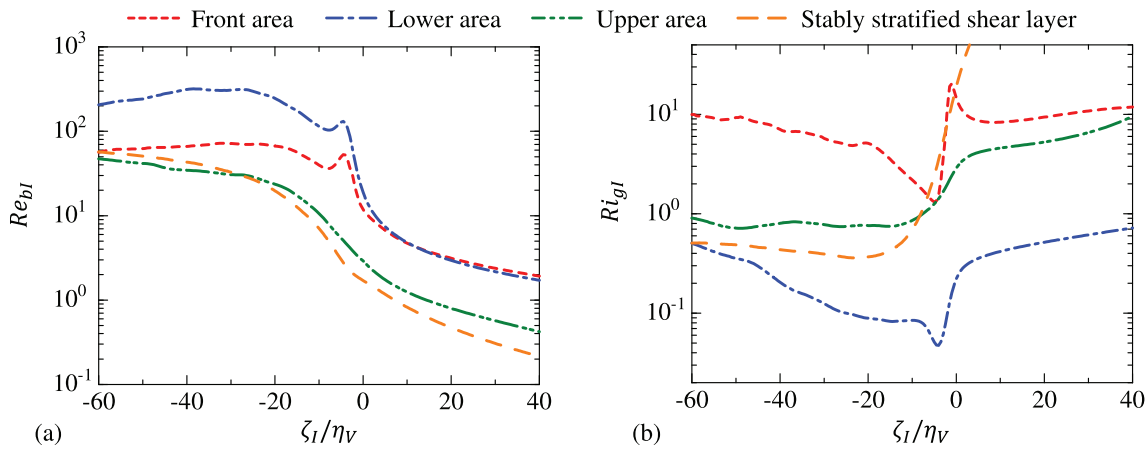


**FIG. 17.** (a) Buoyancy Reynolds number  $Re_{bl}$  and (b) gradient Richardson number  $Ri_{gl}$  near the TNTI layer. Figures also show  $Re_{bl}$  and  $Ri_{gl}$  in the stably stratified shear layer.<sup>13</sup>

patch than in the stably stratified shear layer. A critical value of the gradient Richardson number is  $1/4$  for shear instability in a stratified flow.<sup>33</sup> Except in the turbulent region in the lower area,  $Ri_{gl}$  exceeds this critical value inside the turbulent patch and also in the non-turbulent region. However,  $Ri_{gl}$  near the TNTI layer in the lower region becomes less than  $0.1$ , and the flow region near the TNTI layer can be unstable for the mean shear. The shear instability often results in the formation of large-scale vortices, which can be visualized with negative pressure fluctuations.<sup>34</sup> Figure 18(a) visualizes a two-dimensional profile of pressure fluctuations  $p' = p - \langle p \rangle$ , where the mean pressure is calculated with a spanwise average as  $\langle p \rangle(x, z, t) = \int_{-5}^5 p(x, y, z, t) dy$ . The white line in the figure is the outer edge of the turbulent patch detected with the potential vorticity.

The roller vortex can be identified as large negative pressure fluctuations at  $(x, z) \approx (3, 1)$ , which is close to the outer edge of the turbulent patch. Figures 18(b) and 18(c) visualizes the roller vortex (orange) and small-scale vortex tubes (white) with the isosurface of  $p'$  and  $Q = (\omega_i \omega_i - 2S_{ij}S_{ij})/4$ , respectively, where  $Q$  is the second invariant of the velocity gradient tensor. The pressure isosurface confirms that the spanwise length of the vortex is about  $2h_0$ . The diameter of the roller vortex is larger than the vortex tubes visualized with  $Q$ . In Fig. 18(c), longitudinal vortices are tangled with the roller vortex. It is known that similar longitudinal vortices exist around the roller vortices arising from Kelvin–Helmholtz instability.<sup>35</sup> Taveira and da Silva showed that large-scale vortices appear near the edge of the turbulent region in a turbulent planar jet, and the TNTI layer is formed near the

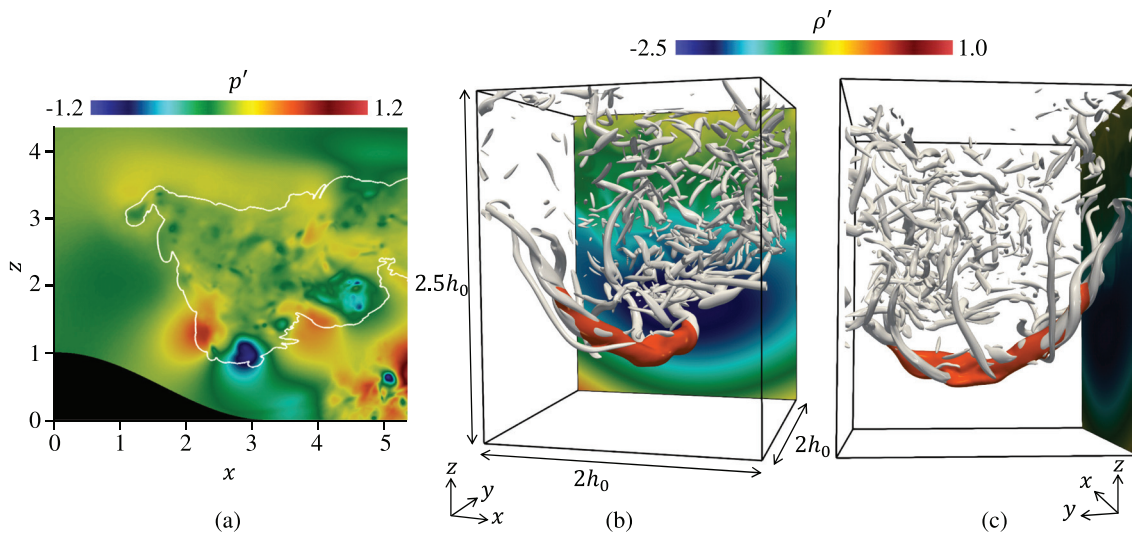


**FIG. 18.** (a) Two-dimensional profile of pressure fluctuations  $p'$  and the outer edge of the turbulent patch. Three-dimensional visualization of isosurfaces of pressure fluctuations  $p' = -1$  and second invariant of the velocity gradient tensor  $Q/(S_j S_j)_V = 80$ : (b) a side view; (c) a view from the upstream region of the turbulent patch.

edge of the vortices.<sup>34</sup> They also found that the large-scale convolutions of the TNTI layer are linked to the presence of the large-scale vortices. This relation between the vortices and the interface geometry is also confirmed in the turbulent patch. The edge of the turbulent patch appears at the perimeter of the roller vortex in Fig. 18(a), and the shape of the turbulent patch is affected by the presence of the vortex. The presence of the roller vortices and the low Richardson number in the lower area in Fig. 17(b) indicate that the TNTI layer in this area behaves similarly to that in non-stratified turbulent free shear flows.

#### IV. CONCLUSIONS

A model of the turbulent patch arising from the internal gravity wave breaking was investigated with direct numerical simulation. The turbulent patch is surrounded by internal gravity waves, where these two regions were successfully distinguished by the potential vorticity. The location of the turbulent patch fluctuates with space and time. However, the turbulence characteristics inside the turbulent patch weakly depend on time. We found that the buoyancy Reynolds number slowly decays and the mixing efficiency stays around 0.2, which is the typical value assumed in oceanography. As also found in turbulent wakes and shear layers in a stably stratified fluid,<sup>12,13</sup> the turbulent patch is separated from the non-turbulent wave region by a thin TNTI layer, whose thickness is about five times the Kolmogorov scale. The kinetic energy dissipation occurs mostly inside the turbulent patch. The potential energy dissipation is more active near the edge of the turbulent patch than in the turbulent core region. The profile of the potential energy dissipation rate near the TNTI layer is consistent with passive scalar dissipation rate in non-stratified turbulent flows.<sup>31,32</sup> The upper area of the turbulent patch is under the strong influence of shear and stable stratification, and a stably stratified turbulent shear layer is formed at the top of the turbulent patch. Therefore, the profile of the buoyancy Reynolds number near the top of the turbulent patch agrees with that in the stably stratified turbulent shear layer.<sup>13</sup> On the other hand, the turbulence in the lower area has large buoyancy Reynolds number. Consequently, the fluid in the lower area is well mixed, and the density gradient becomes small. The difference in the strength of the stratification between the upper and lower areas results in stronger intermittency of the turbulent patch in the lower area. The weak stratification in the lower area also results in a low gradient Richardson number, which is below the critical value for the shear instability near the outer edge of the turbulent patch. The shear instability can lead to the formation of large-scale roller vortices. Indeed, a large-scale roller vortex was found in the lower area. The outer edge of the turbulent patch aligns with the perimeter of the roller vortex, and the spatial distribution of the turbulent patch is influenced by the vortex. The small Richardson number and strong intermittency in the lower area imply that this area resembles non-stratified turbulent free shear flows, where the TNTI layer is also formed at the edge of large-scale vortices.<sup>34</sup>

#### ACKNOWLEDGMENTS

The direct numerical simulation presented in this paper was performed using the high-performance computing system in the Japan Agency for Marine-Earth Science and Technology. This work was also supported by “Collaborative Research Project on Computer Science with High-Performance Computing in Nagoya University” and by JSPS KAKENHI Grant No. 20H05754.

#### DATA AVAILABILITY

The data that support the findings of this study are available from the corresponding author upon reasonable request.

#### REFERENCES

- <sup>1</sup>R. N. Keeler, V. G. Bondur, and C. H. Gibson, “Optical satellite imagery detection of internal wave effects from a submerged turbulent outfall in the stratified ocean,” *Geophys. Res. Lett.* **32**, L12610 (2005).
- <sup>2</sup>H. Wilms, M. Bramberger, and A. Dörnbrack, “Observation and simulation of mountain wave turbulence above Iceland: Turbulence intensification due to wave interference,” *Q. J. R. Meteorol. Soc.* **146**, 3326–3346 (2020).
- <sup>3</sup>A. Melet, R. Hallberg, S. Legg, and K. Polzin, “Sensitivity of the ocean state to the vertical distribution of internal-tide-driven mixing,” *J. Phys. Oceanogr.* **43**, 602–615 (2013).
- <sup>4</sup>C. Wunsch and R. Ferrari, “Vertical mixing, energy, and the general circulation of the oceans,” *Annu. Rev. Fluid Mech.* **36**, 281–314 (2004).
- <sup>5</sup>V. Grubišić and J. M. Lewis, “Sierra wave project revisited: 50 years later,” *Bull. Am. Meteorol. Soc.* **85**, 1127–1142 (2004).
- <sup>6</sup>I. P. Castro and W. H. Snyder, “Experiments on wave breaking in stratified flow over obstacles,” *J. Fluid Mech.* **255**, 195–211 (1993).
- <sup>7</sup>O. S. Eiff and P. Bonneton, “Lee-wave breaking over obstacles in stratified flow,” *Phys. Fluids* **12**, 1073–1086 (2000).
- <sup>8</sup>F. Gheusi, J. Stein, and O. S. Eiff, “A numerical study of three-dimensional orographic gravity-wave breaking observed in a hydraulic tank,” *J. Fluid Mech.* **410**, 67–99 (2000).
- <sup>9</sup>S. N. Yakovenko, T. G. Thomas, and I. P. Castro, “A turbulent patch arising from a breaking internal wave,” *J. Fluid Mech.* **677**, 103–133 (2011).
- <sup>10</sup>C. B. da Silva, J. C. R. Hunt, I. Eames, and J. Westerweel, “Interfacial layers between regions of different turbulence intensity,” *Annu. Rev. Fluid Mech.* **46**, 567–590 (2014).
- <sup>11</sup>J. C. LaRue and P. A. Libby, “Temperature fluctuations in the plane turbulent wake,” *Phys. Fluids* **17**, 1956–1967 (1974).
- <sup>12</sup>T. Watanabe, J. J. Riley, S. M. de Bruyn Kops, P. J. Diamessis, and Q. Zhou, “Turbulent/non-turbulent interfaces in wakes in stably stratified fluids,” *J. Fluid Mech.* **797**, R1 (2016).
- <sup>13</sup>T. Watanabe, J. J. Riley, K. Nagata, R. Onishi, and K. Matsuda, “A localized turbulent mixing layer in a uniformly stratified environment,” *J. Fluid Mech.* **849**, 245–276 (2018).
- <sup>14</sup>G. D. Portwood, S. M. de Bruyn Kops, J. R. Taylor, H. Salehipour, and C. P. Caulfield, “Robust identification of dynamically distinct regions in stratified turbulence,” *J. Fluid Mech.* **807**, R2 (2016).
- <sup>15</sup>S. N. Yakovenko, T. G. Thomas, and I. P. Castro, “Transition through Rayleigh–Taylor instabilities in a breaking internal lee wave,” *J. Fluid Mech.* **760**, 466 (2014).
- <sup>16</sup>Y. Dai, T. Kobayashi, and N. Taniguchi, “Large eddy simulation of plane turbulent jet flow using a new outflow velocity boundary condition,” *JSME Int. J. Ser. B* **37**, 242–253 (1994).
- <sup>17</sup>Y. D. Afanasyev and W. R. Peltier, “The three-dimensionalization of stratified flow over two-dimensional topography,” *J. Atmos. Sci.* **55**, 19–39 (1998).
- <sup>18</sup>T. Watanabe, J. J. Riley, K. Nagata, K. Matsuda, and R. Onishi, “Hairpin vortices and highly elongated flow structures in a stably stratified shear layer,” *J. Fluid Mech.* **878**, 37–61 (2019).
- <sup>19</sup>T. Watanabe and K. Nagata, “Mixing model with multi-particle interactions for Lagrangian simulations of turbulent mixing,” *Phys. Fluids* **28**, 085103 (2016).
- <sup>20</sup>T. Watanabe, X. Zhang, and K. Nagata, “Turbulent/non-turbulent interfaces detected in DNS of incompressible turbulent boundary layers,” *Phys. Fluids* **30**, 035102 (2018).
- <sup>21</sup>H. A. Van der Vorst, “Bi-CGSTAB: A fast and smoothly converging variant of Bi-CG for the solution of nonsymmetric linear systems,” *SIAM J. Sci. Stat. Comput.* **13**, 631–644 (1992).
- <sup>22</sup>Y. H. Tseng and J. H. Ferziger, “A ghost-cell immersed boundary method for flow in complex geometry,” *J. Comput. Phys.* **192**, 593–623 (2003).
- <sup>23</sup>R. R. Taveira, J. S. Diogo, D. C. Lopes, and C. B. da Silva, “Lagrangian statistics across the turbulent-nonturbulent interface in a turbulent plane jet,” *Phys. Rev. E* **88**, 043001 (2013).

- <sup>24</sup>W. D. Smyth and J. N. Moum, "Length scales of turbulence in stably stratified mixing layers," *Phys. Fluids* **12**, 1327–1342 (2000).
- <sup>25</sup>P. J. Diamessis, G. R. Spedding, and J. A. Domaradzki, "Similarity scaling and vorticity structure in high-Reynolds-number stably stratified turbulent wakes," *J. Fluid Mech.* **671**, 52–95 (2011).
- <sup>26</sup>M. C. Gregg, E. A. D'Asaro, J. J. Riley, and E. Kunze, "Mixing efficiency in the ocean," *Annu. Rev. Mar. Sci.* **10**, 443–473 (2018).
- <sup>27</sup>T. R. Osborn, "Estimates of the local rate of vertical diffusion from dissipation measurements," *J. Phys. Oceanogr.* **10**, 83–89 (1980).
- <sup>28</sup>A. Scotti and B. White, "Diagnosing mixing in stratified turbulent flows with a locally defined available potential energy," *J. Fluid Mech.* **740**, 114 (2014).
- <sup>29</sup>D. Krug, M. Holzner, B. Lüthi, M. Wolf, W. Kinzelbach, and A. Tsinober, "The turbulent/non-turbulent interface in an inclined dense gravity current," *J. Fluid Mech.* **765**, 303–324 (2015).
- <sup>30</sup>T. Watanabe, J. J. Riley, and K. Nagata, "Effects of stable stratification on turbulent/nonturbulent interfaces in turbulent mixing layers," *Phys. Rev. Fluids* **1**, 044301 (2016).
- <sup>31</sup>T. S. Silva and C. B. da Silva, "The behaviour of the scalar gradient across the turbulent/non-turbulent interface in jets," *Phys. Fluids* **29**, 085106 (2017).
- <sup>32</sup>K. F. Kohan and S. Gaskin, "The effect of the geometric features of the turbulent/non-turbulent interface on the entrainment of a passive scalar into a jet," *Phys. Fluids* **32**, 095114 (2020).
- <sup>33</sup>P. Hazel, "Numerical studies of the stability of inviscid stratified shear flows," *J. Fluid Mech.* **51**, 39–61 (1972).
- <sup>34</sup>R. R. Taveira and C. B. da Silva, "Kinetic energy budgets near the turbulent/nonturbulent interface in jets," *Phys. Fluids* **25**, 015114 (2013).
- <sup>35</sup>M. Lesieur, *Turbulence in Fluids* (Springer Science and Business Media, 2012), Vol. 40.